MDPI

Article

Efficiency Study of Combined UAS Photogrammetry and Terrestrial LiDAR in 3D Modeling for Maintenance and Management of Fill Dams

Joonoh Kang [1], Daljoo Kim [1], Chulhee Lee [2],[*] , Jaemo Kang [2] and Donggyou Kim [2]

[1] Komapper, Seoul 06097, Republic of Korea
[2] Korea Institute of Civil Engineering and Building Technology, Gyeonggi 10223, Republic of Korea
[*] Correspondence: lch@kict.re.kr

Abstract: Low-cost unmanned aerial system (UAS) photogrammetry and terrestrial laser scanner (TLS, terrestrial LiDAR) technologies are being used as noncontact measurement methods for collecting unstructured data for the maintenance of construction infrastructure facilities. This study investigated the possibility of settlement, which is a maintenance condition evaluation item for fill-dam bodies, using point clouds based on the UAS (unmanned aerial system) structure from motion (UAS-SfM) and TLS (terrestrial laser scanner) point clouds. Specifically, the Z-axis RMSE of the point cloud improved to 0.012 m and the shape reproducibility rate to 98.53% by complementing the heterogeneous data of the UAS and TLS by combining the two systems with block coordination and ICP algorithms. The maximum settlement height and volume (heaving) of the dam crest and upstream and downstream slopes were derived from the combined UAS/TLS point-cloud-based 3D model. The quantitative values for the settlement of the fill-dam body were derived using the combined 3D model with high accuracy and density. This result verified the possibility of using the combined 3D model for evaluation of the maintenance condition.

Keywords: unmanned aerial system; terrestrial laser scanning; point cloud; fill dam; dam maintenance

1. Introduction

Meteorological disasters occur frequently, and the scale of damage of these phenomena is growing because of global climate change. Consequently, aging and degradation of social overhead capital (SOC) infrastructures, such as dams and reservoirs, are accelerating. In particular, approximately 63.5% of reservoirs and dams in South Korea that could cause damage to life and property in the event of a collapse or loss of function are aged 30 years or older [1]. Existing methods (manual visual inspection and document-based work) are problematic as they have limitations for the maintenance and management of aged facilities. Various efforts are being made to overcome these limitations using digital information-based three-dimensional (3D) model reproduction technology for maintenance [2–4]. Spatial density and measurement accuracy in millimeters or centimeters are required to estimate the damage factors of SOC infrastructures [5–8].

Methods such as unmanned aerial system (UAS) photogrammetry and terrestrial laser scanners (TLS, terrestrial LiDAR) are being employed as noncontact measurement technologies for precise 3D point cloud reproductions. The UAS is used for surveying, mapping, topographical mapping, and facility monitoring because of its mobility and fast data acquisition features [9–14]. The image data of a UAS are based on the structure-from-motion (SfM) algorithm. This algorithm can create a 3D point cloud using overlapping images with centimeter-level accuracy [15–20]. The TLS has been used to generate 3D models even before the conception of the UAS [21,22]. The point cloud of the scanned object is recorded through active laser emission. Currently, products with the highest

precision have a measurement error with an accuracy of 2–3 mm and an angle error of 0.5–1" [23–26].

The TLS point cloud and the point cloud from UAS photogrammetry processed on SfM principles have been judged to be equivalent in accuracy [27–30]. However, accuracy issues may arise in the event of missing images, limited overlap ratio, and low spatial resolution resulting from the UAS [5,31–33]. The image quality of a UAS may vary with the camera performance, shooting height, shooting angle, weather conditions, and ground control point (GCP) installation conditions [34–36]. Furthermore, the accuracy of UAS photogrammetry is typically characterized by a higher vertical error of the Z-axis than the horizontal error of the X- and Y-axes [26,37]. In contrast, the TLS offers the advantages of high accuracy and data processing speed, because it enables the collection and direct processing of an exact 3D point cloud of the target via laser. However, accessing the scan target of the TLS is difficult compared to the UAS, and the scan angle is restricted; therefore, drawbacks such as blind spots or data shadows in the point cloud are inevitable [24,38–40]. In particular, the blind spots of vertical structures, such as dams and reservoirs (retaining walls, excavation surfaces, and slopes), have constraints such as blanks resulting from noise-causing vegetation and uneven structures [19,41–44]. Thus, there is a data gap owing to mutual obstruction when utilizing the UAS-SfM or TLS independently [24,45].

Studies have also identified a disparity in the data density and accuracy between point clouds created by the UAS-SfM and TLS. To reduce this disparity, research to mutually supplement heterogeneous data and boost density and accuracy is underway [46]. The iterative closest points (ICP) algorithm [47] is a fine registration technique commonly used to combine two spatially overlapping point clouds. However, the ICP algorithm should be preceded by the coarse registration technique to meet the requirements and be provided with initial values for the overlapping region of the two-point clouds [48].

The following studies were conducted on combined UAS-SfM and TLS point clouds. Ref. [49] investigated the efficacy of overlapping point clouds from the UAS-SfM and TLS for the 3D modeling of the Cheomseongdae pagoda, which is a cultural treasure. Ref. [50] constructed a 3D point cloud for artificial rock walls utilizing the UAS and TLS. Šašak et al. [24] utilized the UAS-SfM and TLS to generate a point cloud and digital elevation model (DEM) for high-resolution mapping and blind-spot reduction in alpine terrains with vertical rock walls and discussed the possible practical implementation thereof. Moon [37] proved that merging earthwork data obtained during building site excavations reduced the vertical inaccuracy along the Z-axis. Ref. [51] employed a fused point cloud to calculate the erosion volume of coastal bedrock. Ref. [52] conducted a comparative analysis on the accuracy and efficiency of calculating the waste stockpile volume using a point cloud that combined the UAS and TLS. Refs. [18,19] demonstrated blind-spot reduction and data accuracy enhancement when using the UAS-SfM and TLS together for landslide monitoring. Another study [26] verified that combining the SfM results of the UAS's camera resolutions at 4K and 8K resolutions with the TLS point cloud improved the accuracy of a 3D point cloud for slopes at 8K resolution [26].

For the maintenance of concrete dams, numerous studies were conducted using either UAS photogrammetry [28,44,50,53–56] or the TLS [22,44,54,57–60]. However, no study has considered the combination of UAS-SfM and TLS point clouds for dam and reservoir maintenance, particularly for fill dams, which account for almost 95% of the total dams and reservoirs in Korea. Consequently, the literature lacks an evaluation of the combination of point clouds from these methods.

In this study, a 3D point cloud for the OO reservoir (fill dam) in Ganghwa-gun, Incheon, Korea, was developed using UAS-SfM-based image processing and a TLS point cloud. To allow for seasonal variations, UAS images were captured in the summer (June) and winter (January) of the following year. GCPs and check points (CPs) were installed for the SfM algorithm of UAS image analysis. Geometric primitives and fast point feature histograms (FPFH) were utilized as coarse registration approaches to merge the point clouds of the UAS-SfM and TLS, and the ICP algorithm was employed as a fine registration step.

The aim of this study was to review the efficiency of utilizing a 3D point cloud generated by combining UAS-SfM and TLS point clouds for the maintenance assessment of fill dams. First, the global navigation satellite systems' (GNSS) survey checkpoints were compared in the UAS-SfM and TLS 3D point clouds, and the accuracies were compared and examined using the root-mean-square error (RMSE) of the X-, Y-, and Z-axes, as well as the shape reproducibility rate based on the data gap. Furthermore, subsidence and deformation, which are damage factors for dam and reservoir maintenance, were analyzed and reviewed using the 3D point cloud developed by combining the UAS-SfM and TLS point clouds.

2. Materials and Methods

2.1. Experimental Area

The OO reservoir is located in Ganghwa-gun, Incheon, South Korea. This reservoir with a height of 21.5 m and a length of 640 m was constructed in 1989 (zone type: fill dam). Table 1 lists the detailed specifications. The reservoir is a facility subject to maintenance inspection in accordance with the Special Act on the Safety Control and Maintenance of Establishments [61]. The facility is currently in good condition, with a total grade of B. The upstream slope has crushed stone protection, while the downstream slope has surface protection in the form of vegetation to avoid erosion caused by water level variations. Private dwellings and farmland are distributed in the lower reaches of the reservoir for farming (Figure 1).

Table 1. Dam specifications of OO reservoir.

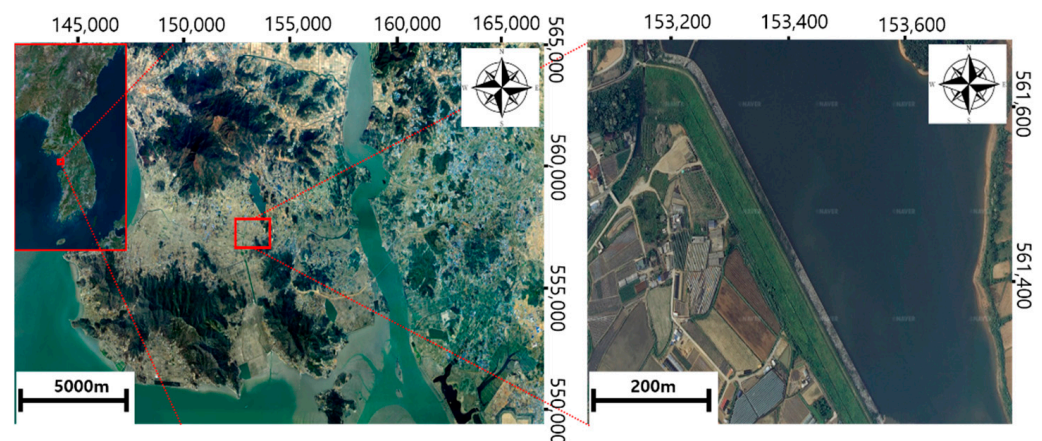| Type	Height (m)	Length (m)	Dam Crest Width (m)	Gradient of Upstream Slope	Gradient of Downstream Slope	Full Water Level (EL.m)	Dead Storage Level (EL.m)
Fill dam (zone type)	21.5	640	6	1:2.2	1:2.0	28.5	14

Figure 1. Location of the study site: OO reservoir, Ganghwa-gun, Incheon, South Korea.

2.2. Method Workflow

Vegetation on the downstream slope of the OO reservoir was employed to protect the surface from external factors. It might obstruct the detection of ground surface changes via UAS photogrammetry and TLS survey [26,62]. Considering the vegetation distribution in summer, which is a seasonal factor, we deemed necessary the examination of the relationship between the GCP accuracy and the settlement and deformation of the ground's surface. Therefore, the UAS images were captured in summer (June) and winter (January) and then compared. A TLS survey was conducted in winter (January) to minimize the interference of vegetation. The point clouds of UAS-SfM and TLS obtained in winter were combined. Furthermore, the possibility of maintenance via a combination of UAS-SfM and

TLS was reviewed by deriving quantitative values for the settlement visually observed on the downstream slope and dam crest. The workflow of the 3D point cloud produced using UAS and TLS data is illustrated in Figure 2.
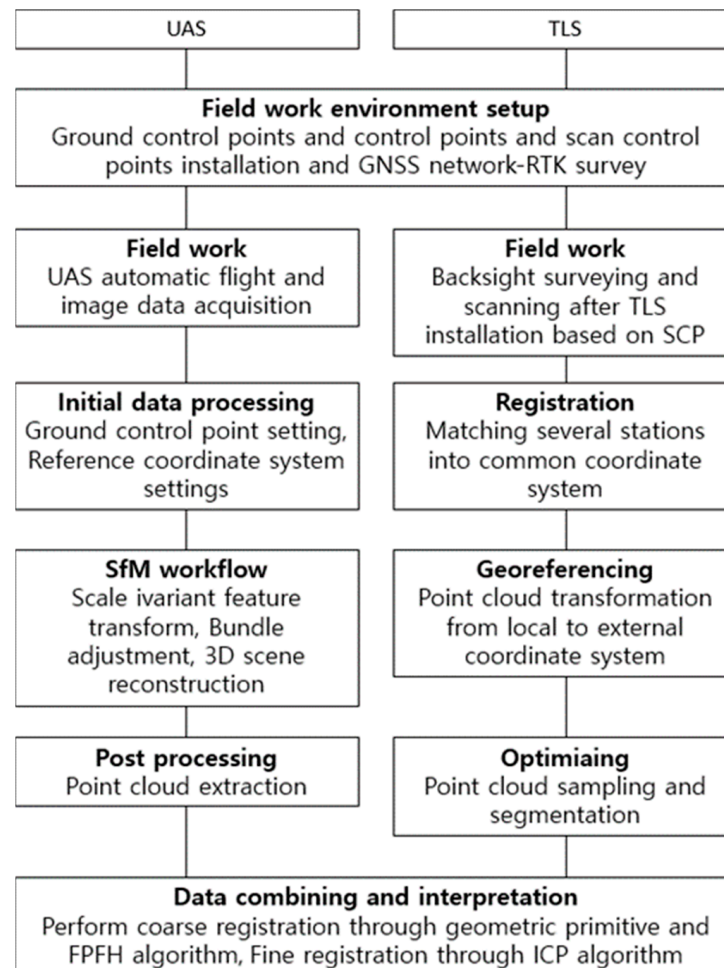

Figure 2. Workflow of the developed 3D point cloud.

2.3. Data Acquisition

The location attributes and geotagging of digital images are required to apply the SfM algorithm to the images captured by the UAS [48,63]. This is because the camera position derived from the SfM algorithm does not have the scale and direction provided by the GCP coordinates [31]. Thus, for the precise measurement of the GCPs, such as the actual ground information, network real-time kinematic (RTK) GNSS surveys were conducted for 10 GCP reference points and 7 CPs to verify the position accuracy using the Trimble GNSS R8 satellite signal receiver (Figure 3). UAS photogrammetry was executed both in summer (June) and winter (January) to distinguish trends according to the seasonal changes in vegetation in the fill dam. The UAS used in this study was the AUTEL's EVO2 Dual 640 T mounted with a Robotics XT701 camera with 8 K (8000 × 6000) resolution, 1/2 CMOS image sensor, and lens with an of FOV of 79° and a focal length of 4.3–17.2 mm through lossless 4× optical zoom. For the TLS, we used the Trimble laser scanner SX10 equipped with time-of-flight (ToF) technology suitable for building 3D point clouds with a 5MP resolution and band scanning technology for precise scanning. Laser scanning with an effective range of 600 m, a scanning angle accuracy of 1″, and a distance measurement accuracy of 1 mm + 1.5 ppm was achieved. The detailed specifications of the equipment used to produce the 3D point cloud of the OO reservoir are summarized in Table 2.
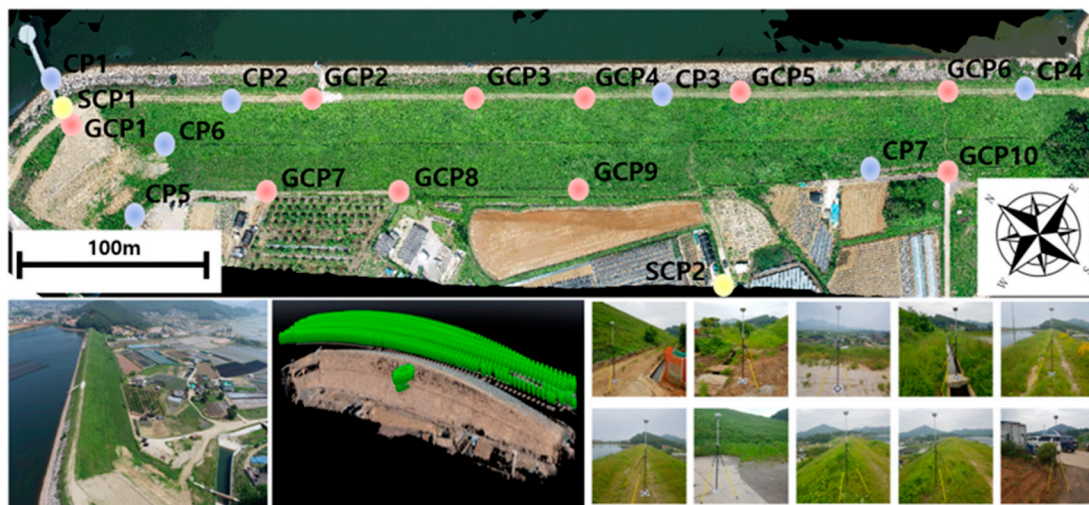
Figure 3. Network RTK: Trimble GNSS R8. (GCP: points for inputting geographic information to UAS-based image analysis; CP: points for UAS-based video interpretation accuracy review; SCP: TLS install point.)

Table 2. GNSS, UAS, and TLS specifications.

Trimble GNSS R8	Parameters			
	Weight	1.52 kg	Channel	440 Channels
	Stop Positioning Vertical	3.5 mm + 0.4 ppm RMS	Input	CMR+, CMRx, RTCM2.1–3.1
	Stop Positioning Horizontal	3 mm + 0.1 ppm RMS	Output	24 NVEA
	VRS Vertical	15 mm + 0.5 ppm RMS	Radio Modem	403 MHz
	VRS Horizontal	8 mm + 0.5 ppm RMS	Signal Update Cycle	1–20 Hz
AUTEL EVO2	**Parameters**		**Camera**	
	Weight	1110 g	Resolution	8000 × 6000
	Satellite System	GPS/GLONASS/Galileo	Image Sensor	1/2 CMOS
	Max Flight Time	42 min	ISO	100–3200 (auto)
	Angular Vibration Range	±0.005°	F-Stop	F/1.8
Trimble SX10	**Parameters**			
	Angle Accuracy	1″	Range Noise	1.5 mm
	Accuracy	Prism: 1 mm + 1.5 ppm DR mode: 2 mm + 1.5	EDM	Laser: 1550 mm Laser spot size at 100 m: 14 mm
	Scanning	Band Scanning	Point Spacing	6.25–50 mm
	Measurement Rate	26.6 kHz	Camera	5MP (84×)
	Range	Prism: 5500 m DR Mode: 800 m	Communication	Wi-Fi, USB, Cable, Long range radio

2.4. UAS Photogrammetry

The UAS images were captured by the AUTEL EVO2 in June 2020 (summer) and January 2022 (winter). The device auto-acquired 962 images under the same shooting conditions via automatic flight (altitude = 100 m, vertical and horizontal overlap = 85%, camera angle of 90°, normal speed) using the Pix4D Capture app. The camera was also changed to an angle of 60° and an altitude of 70 m, and 69 images were manually captured

while the drone flew along the slope of the fill dam (longitudinal overlap = 75%). Thus, 1031 images were acquired for June 2020 and January 2022, respectively. The ground sample distance for the captured image is 1.7 cm/pixel based on flight height. A high degree of image overlap is required to reproduce a 3D point cloud with the SfM algorithm, and it is generally set to 60–80% [64–66]. In this study, images were shot with an overlap level of approximately 80%. When the SfM algorithm was applied, scale and directional information were obtained using a small number of GCPs located on the ground, which were clearly visible in each image. Consequently, a 3D point cloud was created in the relative coordinates with reference to the image coordinate system [31]. In photogrammetry, accuracy is usually evaluated based on a statistical RMSE, in which the GCP is used as an important parameter [67]. Regarding the discrepancy between the 3D point cloud and the CP, the accuracy is evaluated using the RMSE of the two axes (X, Y) parallel to the ground and vertical z coordinates [68]. The GCPs must be uniformly distributed throughout the survey area, and the topography's morphology must be considered [62,69]. Therefore, in this study, four GCPs were set on the lower part of the downstream slope and six on the dam crest. In addition, seven CPs were set as the accuracy checkpoints. The point-cloud accuracy of the UAS-SfM was evaluated by measuring these CPs based on the GNSS field survey.

2.5. TLS Survey

Setting of the optimal scanner position is crucial to creating a TLS-based point cloud [64,70]. When positioning the scanner, data gaps and shadows must be as minimized as possible considering the solidity and accessibility of the terrain, and the point clouds of the two positions must overlap [19]. Scan control points (SCPs) were placed at the bottom of the downstream slope of the fill dam and at the dam crest, so that the GCPs and CPs could be measured at the scanning positions. For the TLS survey, the GNSS network RTK survey was performed at two SCPs using the Trimble laser scanner SX10, and a light detection and ranging (LiDAR) scan was performed using the SCPs as station marks. The point cloud accuracy of the TLS was also measured and evaluated at the set CPs based on the GNSS field survey.

2.6. Combination of UAS-SfM and TLS Point Clouds

The data gaps, blind spots, and data shadows that exist independently for each measurement technique can be reduced by fusing the acquired UAS-SfM and TLS point clouds. TLS data allow for mutual complementation at a higher level of accuracy than the UAS-SfM point cloud. Furthermore, the UAS-SfM data can acquire realistic images by reducing the blind spots and data shadows of the TLS according to terrain, slope, and scan position [19]. Consequently, we presumed that a 3D point cloud of the fill dam with a high level of accuracy could be produced and utilized for maintenance.

To combine the point clouds, the image captured by the UAS was first converted into a 3D point cloud using the SfM with Pix4Dmapper professional software. In the preprocessing step, Pix4Dmapper automatically extracted the junctions centered on the image unit features and matched them with multiple adjacent images. A 3D model was developed by computing the exterior orientation parameters, for which relative orientation parameters were calculated by analyzing the essential or fundamental matrices. Aerial triangulation (AT) was performed based on WGS84, a coordinate system applied to the image, which is an auxiliary tool for calculating the relative orientation parameters. After extracting and matching the feature points, the output coordinate system of the 3D point cloud was projected to a geoid height of +22.115 m for Korea2000/Central Belt 2010 (EPSG: 5186) and GRS80. Thereafter, orthographic projection based on the absolute coordinates was performed on the 3D model, and a 3D point cloud was established through dense matching.

The point cloud of the TLS, including the coordinates in the scanning process, was acquired. After entering the station coordinates and prism point coordinates of the TLS using the SCP, the position and azimuth of TLS were set by collimating the prism. In

addition, all objects were scanned at a 360° orientation using the ToF technique, which measures the distance using the time taken by the laser to be reflected and return to the object. The scan coordinates were calculated in real time to generate the applied point cloud. Data were optimized using Trimble Realworks.

The two-point clouds were combined in two steps: coarse registration and fine registration. The independently acquired UAS and TLS point clouds are formed based on their respective coordinate systems; hence, spatial offsets occur during fusion [19]. Hence, coarse registration, which can incorporate the correct positioning of the coordinate system required for the point cloud, is necessary (Wu et al., 2020). Therefore, in this study, UAS-SfM and TLS heterogeneous point clouds were registered using geometric primitives. A data bundle was divided into multiple data blocks, and coarse registration was performed by adjusting each point through the FPFH algorithm, focusing on the main feature points. For each block, fine registration was performed to minimize the 3D distance between the points by transforming or rotating the entire point cloud along the X-, Y-, and Z-axes using the ICP algorithm based on TLS coordinate data [24].

3. Results

3.1. Evaluation of Accuracy and Reproducibility of UAS 3D Point Cloud

The GCP is an important parameter associated with image quality. The number of GCPs is correlated with image quality improvement [61]. GCP is the reference point for the UAS-SfM, and CP is the checkpoint. Both types of survey points were measured based on the Korea2000/Central Belt 2010 (EPSG: 5186) coordinate system. To evaluate the accuracy of the UAS-SfM point cloud, we measured the x, y, and z values of the ten GCPs listed in Table 3 and seven CPs installed close to vegetation.

Table 3. Measured value of GCP and CP via RTK.

Type	Point	X	Y	Z
GCP	1	153,220.641	561,642.718	32.480
	2	153,306.828	561,542.339	32.065
	3	153,363.307	561,465.100	32.112
	4	153,402.628	561,412.542	32.284
	5	153,443.243	561,351.401	32.064
	6	153,516.883	561,254.436	32.092
	7	153,255.305	561,526.634	11.677
	8	153,296.481	561,471.640	11.734
	9	153,366.399	561,382.430	12.423
	10	153,479.991	561,229.526	15.968
CP	1	153,227.739	561,649.956	32.030
	2	153,270.594	561,589.408	32.170
	3	153,427.131	561,378.978	32.183
	4	153,555.267	561,201.412	32.094
	5	153,215.190	561,561.309	13.125
	6	153,230.306	561,602.811	22.458
	7	153,452.354	561,264.400	14.225

Figure 4a depicts the 3D point cloud created with the UAS-SfM point cloud in summer (June). The model was generated based on 220 million points in the point cloud. Figure 4b shows a 3D point cloud created with the SfM using images captured by UAS in winter (January). This model was composed of 218,004,114 point clouds. The presence or absence of vegetation is clearly contrasted when viewed with the naked eye. The degree of influence of vegetation was compared using cross-sectional views based on the GNSS surveys obtained before capturing the UAS images. Figure 4c compares the cross-sectional views of the same point in the 3D point clouds produced in summer and winter based on those of the visual survey report. In summer data, vegetation caused an erratic increase in elevation, whereas in the winter data, this difference was minimal and exhibited a gentle shape.
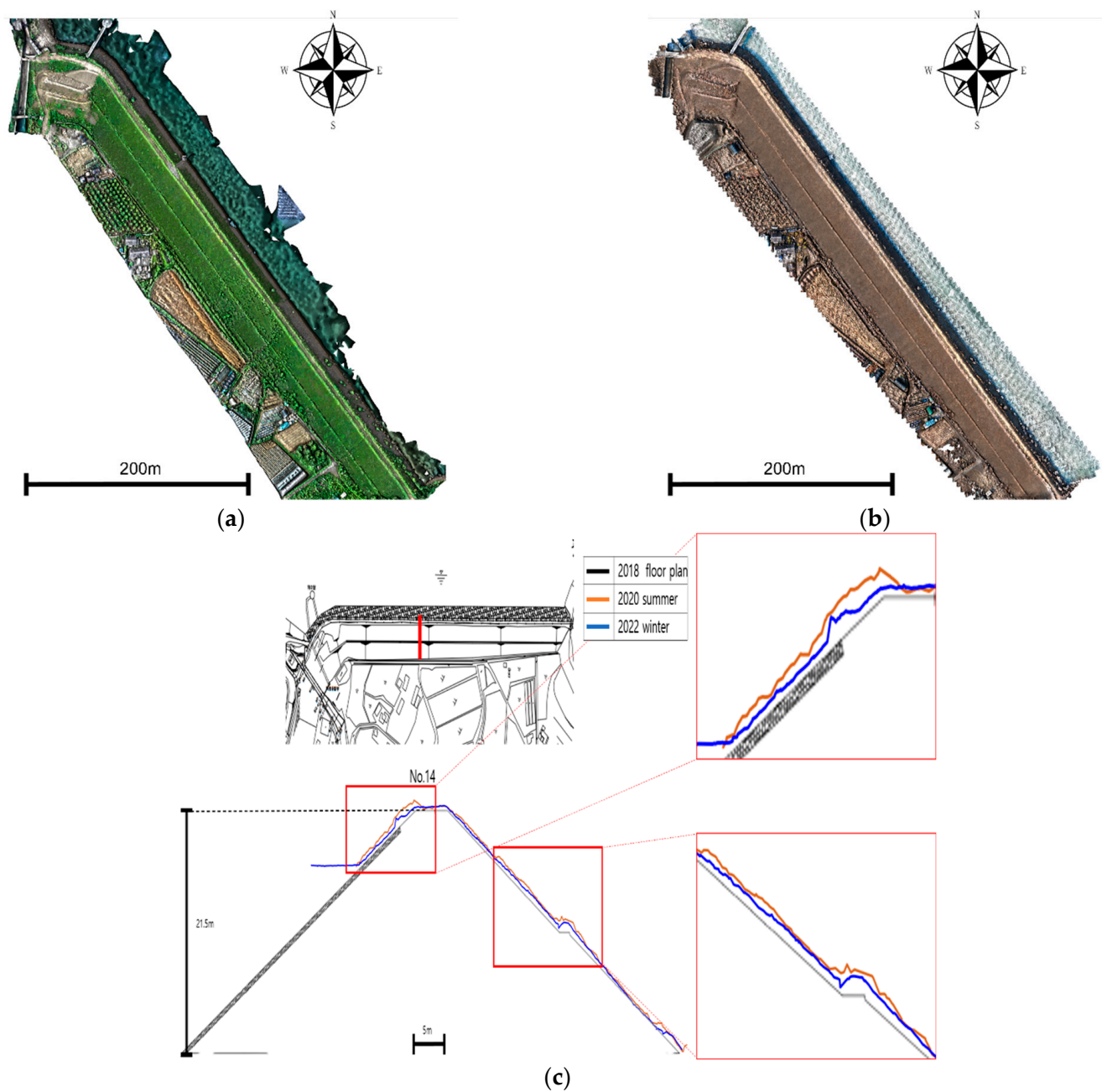
Figure 4. (**a**) Summer UAS image analysis conducted in 2020. (**b**) Winter UAS image analysis conducted in 2022. (**c**) Comparison of cross-sections from 2018, 2020, and 2022.

Table 4 lists the CP error value and RMSE coordinates of the 3D point cloud developed using the UAS-SfM in summer. Table 5 lists the CP error value of the 3D point cloud developed using the UAS-SfM in winter. Both the summer and winter data exhibited a larger error along the Z-axis than along the X- and Y-axes. The Z-axis error in summer was 0.110 m, which was twice that in winter (0.057 m). In the summer of 2020, the error in the Z-axis of the point cloud occurred in various numbers, and in the winter of 2022, the error in the Z-axis of the point cloud was -, confirming that an error occurred in one direction.

Table 4. CP error value and RMSE for summer 2020 via UAS-SfM (unit: m).

Type	Point	X	Y	Z
CP error value	1	0.009	−0.003	0.138
	2	0.012	0.012	0.242
	3	−0.008	0.010	0.006
	4	−0.022	0.020	−0.044
	5	−0.021	−0.011	0.025
	6	−0.019	−0.015	−0.044
	7	−0.020	−0.012	−0.056
RMSE		0.017	0.013	0.110

Table 5. CP error value and RMSE for winter 2022 via UAS-SfM (unit: m).

Type	Point	X	Y	Z
CP error value	1	0.005	0.010	−0.061
	2	0.016	−0.004	−0.058
	3	0.003	0.012	−0.059
	4	0.020	−0.011	−0.057
	5	0.016	0.012	−0.052
	6	0.032	0.005	−0.055
	7	0.012	0.021	−0.054
RMSE		0.017	0.012	0.057

In the summer of 2020, the error in the Z-axis of the point cloud occurred in various numbers, and in the winter of 2022, the error in the Z-axis of the point cloud was -, confirming that an error occurred in one direction. In general, the error in UAS photogrammetry proceeds in one direction. As a result of the analysis, the vegetation that grew tall was shaken by the wind during UAS shooting, and the location in the image appeared irregular. As a result, it is thought that an error occurred due to the influence of vegetation in the image analysis AT process.

Figures 5 and 6 reveal the shape reproducibility of the 3D point cloud in winter used to identify gaps in the point cloud. The total area of the fill dam measured by the UAS-SfM point clouds in summer and winter was 37,503.706 m^2. Points that are more than 3 m above the height of the dam crest and slope were manually deleted. The empty space of the data was manually measured to calculate the area where the fill dam was not reproduced. The UAS-SfM in summer revealed that the area occluded by vegetation removal on the upper and lower slopes was 572.464 m^2, with a shape reproducibility rate of 98.47%. In winter, the UAS-SfM revealed the area blocked by vegetation removal on the upper slope was 551.305 m^2, with a shape reproducibility rate of 98.53%.

3.2. Evaluation of Accuracy and Reproducibility of TLS 3D Point Cloud

The TLS and UAS-SfM point clouds were compared to determine the area blocked during TLS (Figure 7). An occluded area appeared at the point in Figure 7a, because the upstream slope could not be scanned owing to the limit of the TLS scanning angle. The dam crest data near SCP1, which is a TLS station installed on the dam crest, could be acquired. However, when acquiring data on the same plane as the laser scanning direction, a blocked area was generated with increasing distance because of the TLS characteristic that involved multiple blanks generated by the scanning angle. The point in Figure 7b is on the downstream slope, where a blocked area appeared because of the laser scanning direction from SCP01 and the buildings and other obstacles from SCP02. At the point in Figure 7c, an area was occluded by trees located between SCP02 and the downstream slope. By generating the 3D point cloud with a TLS, because of the area without data, the shape reproducibility was calculated as 74.59%, which was lower than that of UAS-SfM point cloud shape reproducibility.
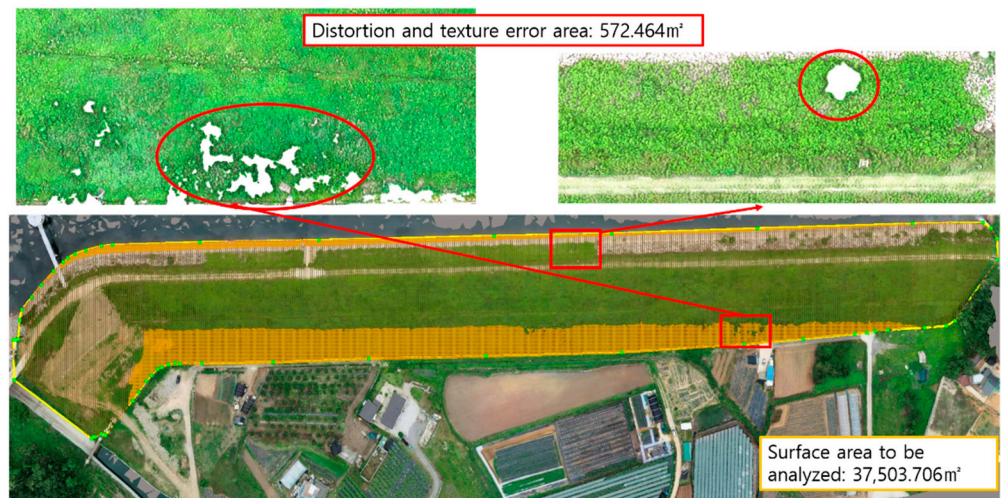
Figure 5. Shape reproducibility of the UAS-SfM 3D in summer.

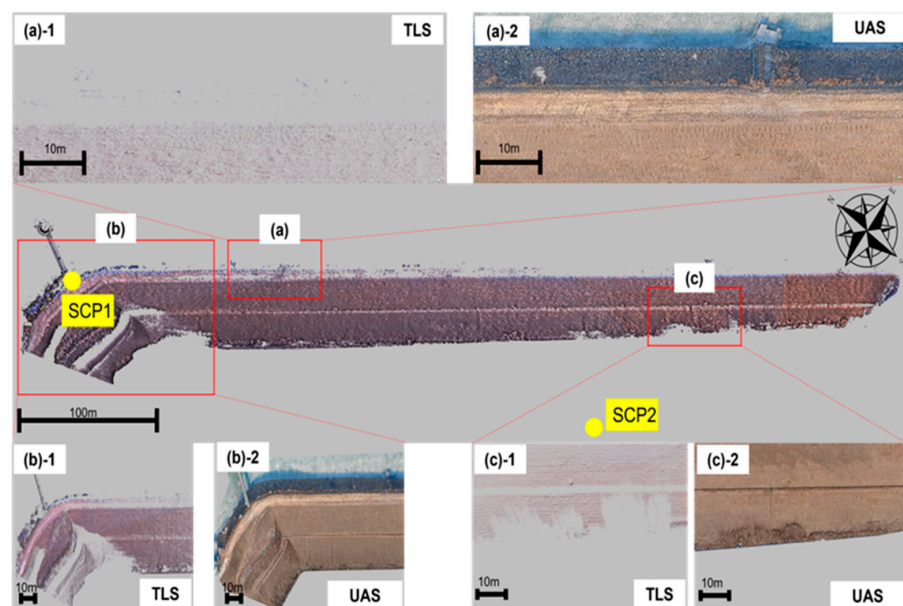**Figure 6.** Shape reproducibility of the UAS-SfM 3D in winter.

Figure 7. (**a**) Blind spot comparison of TLS and UAS-SfM in dam crest and upstream slope regions. (**b**) blind spot comparison of TLS and UAS-SfM near SCP01 (**c**) blind spot comparison of TLS and UAS-SfM on the downstream slope.

Table 6 lists the CP error value coordinates measured by the TLS. CPs 3 and 4 could not be detected because of data gaps. The coordinates of some CPs were missing because the TLS scan area was smaller than the UAS flight area. For CPs 1, 2, 5, 6, and 7, the RMSE was calculated by comparing the coordinates obtained via the network RTK GNSS survey with the CPs measured via the TLS. Although the shape reproducibility of the 3D point cloud was lower than that of the UAS-SfM, the Z-axis RMSE was 0.012 m; thus, the 3D model was found to have a higher accuracy than the UAS-SfM.

Table 6. CP error value and RMSE via TLS (Unit: m).

Type	Point	X	Y	Z
	1	0.012	0.009	0.006
	2	0.012	0.016	−0.013
CP error value	3	-	-	-
	4	-	-	-
	5	0.014	0.016	−0.012
	6	0.018	0.013	−0.014
	7	0.022	0.016	−0.011
RMSE		0.016	0.014	0.012

3.3. Evaluation of the Accuracy and Reproducibility of UAS–TLS 3D Point Cloud

Based on the TLS point cloud in Figure 8b, we load the UAS-SfM point cloud in the same coordinate system. In the process of triangulation, each bundle is decomposed based on the blocks created for point cloud construction, and blocks are adjusted based on three or more artificial structures that can be used as fixed points in the point cloud within block adjustment and, with the man-made structure forcibly restrained, comprehensive coordination is performed through the ICP algorithm. AT was performed by combining the UAS-SfM point cloud displayed in Figure 8a and the coordinates of the TLS point cloud shown in Figure 8b. Subsequently, a combined point cloud was created through the block adjustment of each bundle (UAS, TLS), as presented in Figure 8c.

The red and green dots in Figure 9 represent the TLS and UAS-SfM point clouds, respectively. Figure 9a shows the analysis area. Figure 9b highlights the point clouds of the dam crest before combination. Figure 9c shows the point cloud of the dam crest after combination. Figure 10 compares the cross-section of the 2018 floor plan and the 2022 combined model. Areas with high growth of some vegetation have protruded cross-sections. Moreover, settlement and heaving can be seen on the downstream slope. The coordinates of the X- and Y-axes of the UAS-SfM point clouds were optimized via bundle block adjustment based on the point cloud coordinates of the TLS. In contrast, the Z-axis coordinate with a large RMSE error was adjusted rather coarsely. Table 7 lists the CP error value of the combined data, and the RMSE was calculated by comparing them with the CPs obtained via the network RTK GNSS survey. The Z-axis coordinate error of the UAS-SfM was corrected. Furthermore, the shape reproducibility of the dam body including the upstream and downstream slopes and dam crest of the combined data was 98.53%, indicating that the shape reproducibility of TLS was enhanced.

Table 7. CP error value and RMSE for the combined model (unit: m).

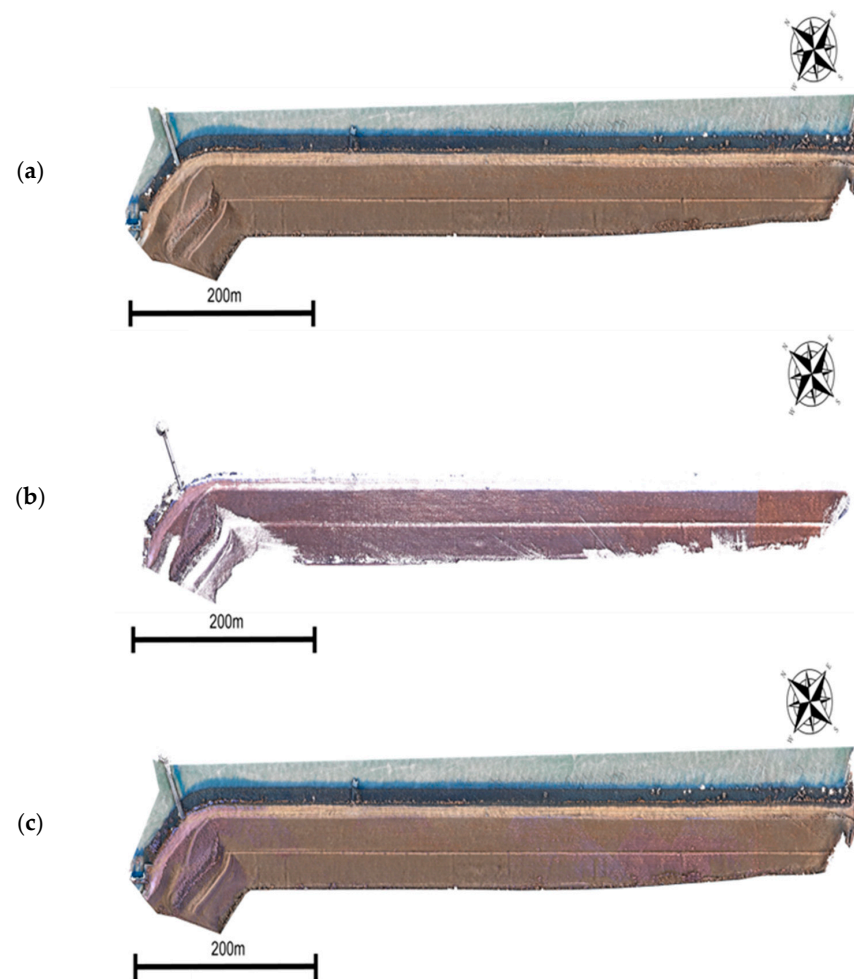| Type	Point	X	Y	Z
	1	0.005	0.006	0.005
	2	0.012	0.016	−0.013
	3	0.001	0.006	−0.017
CP error value	4	0.008	−0.004	−0.007
	5	−0.004	0.007	−0.009
	6	0.018	0.013	−0.014
	7	0.022	0.016	−0.011
RMSE		0.012	0.011	0.012

Figure 8. (**a**) UAS-SfM point cloud, (**b**) TLS point cloud, and (**c**) combined point cloud.
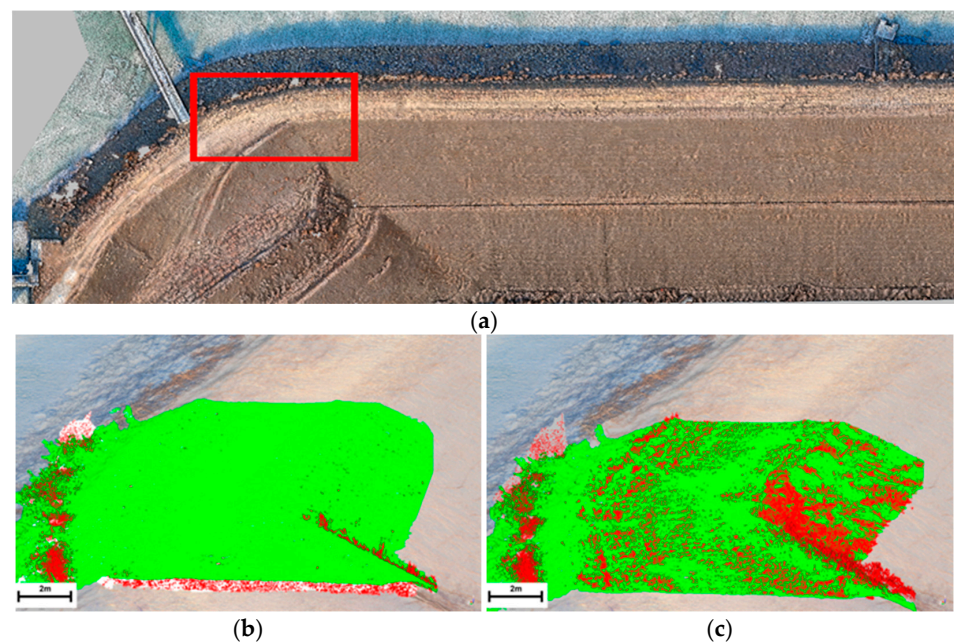

Figure 9. (**a**) Area of analysis. (**b**) UAS-SfM and TLS point clouds of the dam crest before combination. (**c**) UAS-SfM and TLS point clouds of the dam crest after combination.
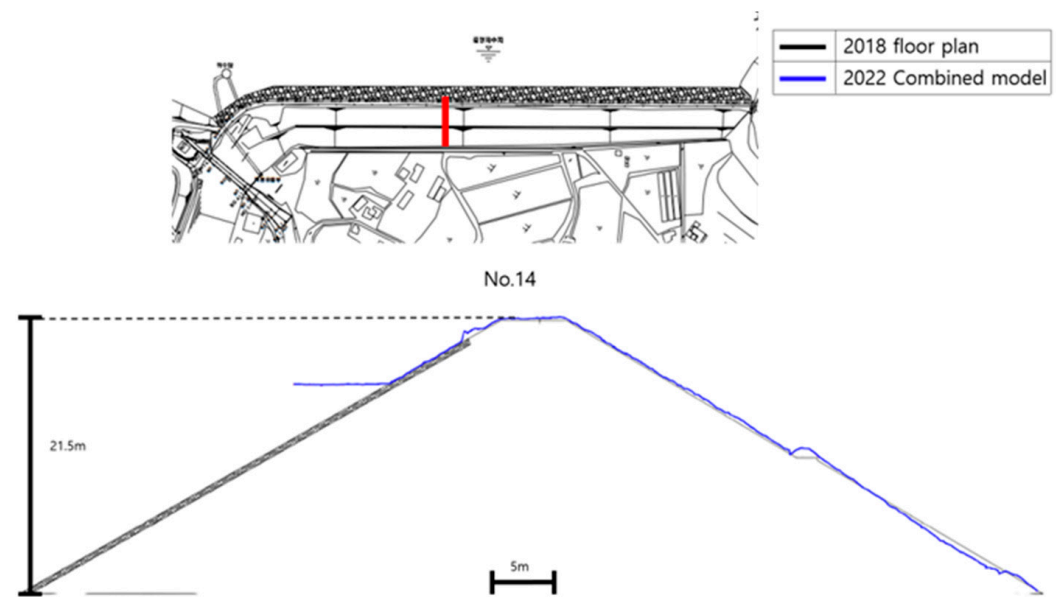
Figure 10. Comparison of cross-sections from 2018 floor plan, 2022 combined model.

3.4. Displacement Detection

The settlement of dams and reservoirs is measured by contact survey using survey staff and poles in the field. In contrast, the UAS and TLS measure the settlement through post-processing after acquiring image and scan data in the field. Displacement can be detected once time-series data have been accumulated. Thus, settlement (heaving) was detected in the 3D point cloud based on the combination analysis using a contact-survey-based cross-sectional view. The measurement criteria are the values measured by the GNSS survey before the UAS and TLS surveys, as displayed in Figure 4c. The displacement was detected through a comparison with the 3D point cloud combining the UAS and TLS point clouds scanned in winter.

Table 8 presents the detected volume and maximum height of seven settlements and heaving of the dam crest in the 3D point cloud combining UAS-SfM and TLS point clouds. In the Crest-A section, a local settlement occurred in the area adjacent to the upper slope. In contrast, the shape revealed that heaving had occurred in the direction of the downstream slope, and the measured heaving volume was 9.331 m^3. In the Crest-B section, the settlement volume was 11.84 m^3, and the maximum settlement height was 0.205 m. From the Crest-C to Crest-G sections, the maximum settlement height was 0.15–0.20 m, and the maximum heaving height was 0.11–0.26 m. This reveals an uneven ground surface where settlement and heaving coexist. If the maximum settlement and elevation are 0.206 and 0.266 m, respectively, as in Crest-F, the settlement height might be incorrectly measured as 0.472 m when the settlement measurement is based on the elevation of the existing contact type survey. However, the 3D point cloud of this study exhibited high accuracy, with a Z-axis RMSE of 0.012 m. Therefore, when the settlement/heaving height is 0.2 m, it has a high reliability within the allowable range of measurement error, and the model reflects the characteristics of the irregular elevation of the ground surface.
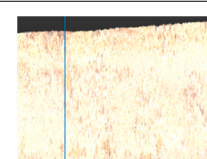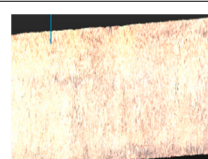
Table 8. Dam crest displacement data.
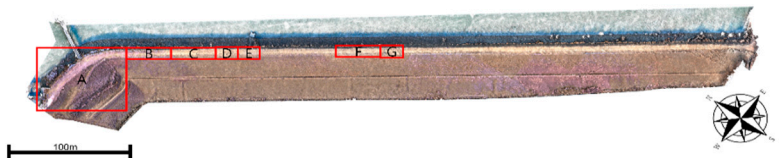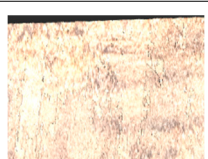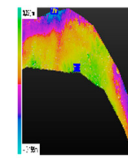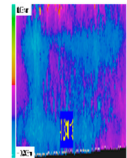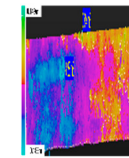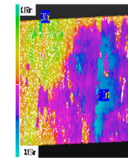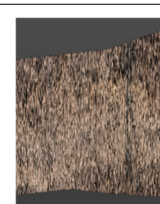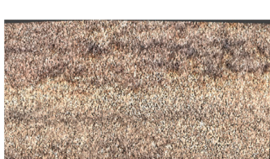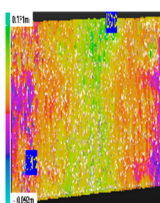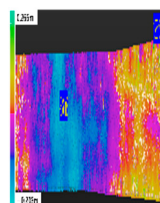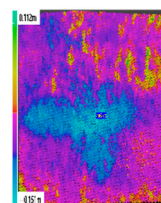
Type	A	B	C	D
Subsidence Area				
Inspection Map				
Length (m)	67	18	24.5	12.5
Settlement Volume (m^3)	1.976	11.840	3.238	1.167
Heaving Volume (m^3)	9.331	0.040	0.313	0.580
Maximum Height of Settlement (m)	0.159	0.205	0.183	0.163
Maximum Height of Heaving (m)	0.220	0.054	0.149	0.163
Type	**E**	**F**	**G**	
Subsidence Area				
Inspection Map				
Length (m)	20	51	7.4	
Settlement Volume (m^3)	0.137	8.861	1.059	
Heaving Volume (m^3)	1.693	1.285	0.060	
Maximum Height of Settlement (m)	0.092	0.206	0.151	
Maximum Height of Heaving (m)	0.171	0.266	0.112	

Table 9 lists the detection results for four settlements and heavings on the upstream slope. A crushed stone surface protection exists on the upstream slope to prevent erosion and loss due to water level changes. Unlike the dam crest, there was a relatively large elevation difference between the settlement and heaving because it was in contact with the water. In the Upstream-B, -C, and -D sections, the settlement volume was approximately 13.46–25.28 m^3, the maximum settlement height was 0.29–0.418 m, and the maximum elevation was 0.51–0.42 m. The inspection map reveals that settlement occurred in the section adjacent to the water. A heaved shape appeared in the section adjacent to the dam crest. In the Upstream-C and -D sections, areas where data gaps occurred because of interference from vegetation are displayed in black.
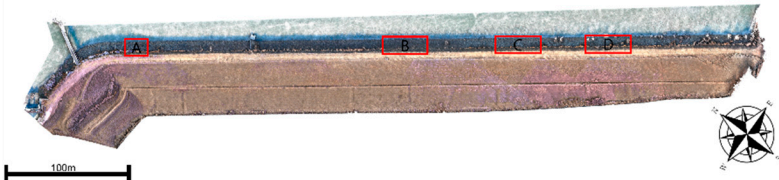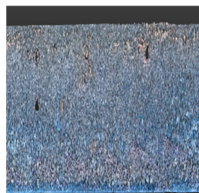
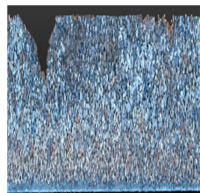**Table 9.** Upstream slope displacement data.
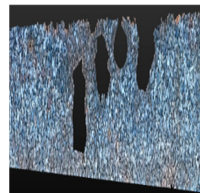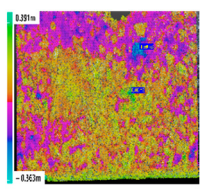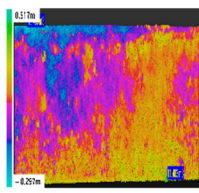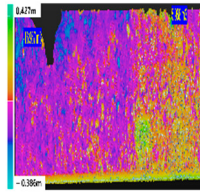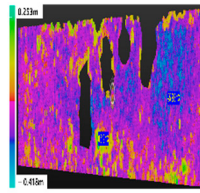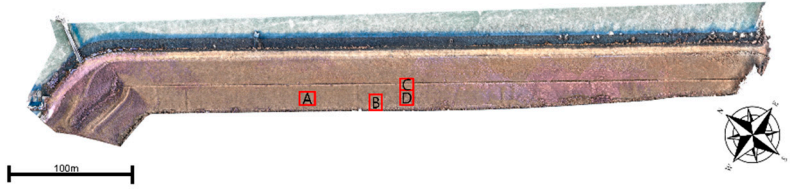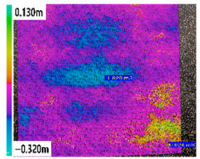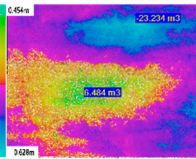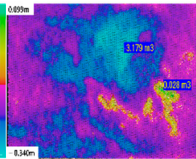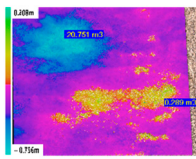
Type	A	B	C	D
Subsidence Area				
Inspection Map				
Length (m)	20	38.7	20	41
Settlement Volume (m^3)	1.556	13.468	16.967	25.283
Heaving Volume (m^3)	5.396	11.483	5.958	0.619
Maximum Height of Settlement (m)	0.363	0.297	0.386	0.418
Maximum Height of Heaving (m)	0.391	0.517	0.427	0.253

Table 10 lists the four settlements and heavings that occurred on the downstream slope of the combined point cloud. It is difficult to determine the degree of settlement and heaving in the image. However, when the altitude difference was checked using the inspection map, settlement volumes of 23.234 and 20.751 m^3 were obtained for the Downstream-B and -C sections. Their maximum settlement heights were 0.628 and 0.756 m, respectively, and their maximum heaving heights were 0.454 and 0.208 m, respectively. A bulging shape was detected. To determine the cause of settlement and heaving, previous data must be compared, or the history of the relevant area must be managed. However, it is difficult to compare the measured values of this study with the results of previous investigations because they are the result of the contact investigation. It is possible to indirectly estimate the erosion by using the seepage line through the leakage at the bottom

of the downstream slope, but no trace of leakage was found during the winter survey. The data can however be used as the initial values of the time history for the degree of occurrence of damage factors in future investigations.

Table 10. Downstream slope displacement data.

Type	A	B	C	D
Subsidence Area				
Inspection Map				
Length	4 m	14.5 m	6.8 m	11 m
Settlement Volume	3.179	23.234	1.828	20.751
Heaving Volume	0.028	6.484	0.024	0.289
Maximum Height of Settlement	0.320 m	0.628 m	0.340 m	0.756 m
Maximum Height of Heaving	0.130 m	0.454 m	0.099 m	0.208 m

4. Discussion

The effectiveness of UAS-image- and TLS-based 3D data for fill-dam maintenance using 3D modeling was reviewed based on the analysis results presented above.

Regarding coordinate accuracy, 3D data of a large area can be rapidly acquired from image data. However, the accuracy is determined by the overlapping and resolution of the images and the error of correction elements inside and outside the camera. The accuracy of UAS photogrammetry had an RMSE of 0.057 m, which is 0.045 m higher than the Z-axis coordinate accuracy of the TLS. It is attributed to the vertical error of the Z-axis being higher than the horizontal error of the X- and Y-axes [26,37]. This outcome presented an obstacle to the investigation of the settlement and upheaving of the fill dam. However, the Z-axis RMSE was found to have been enhanced to 0.012 m when combined with the TLS point clouds, which provided a higher density and accuracy than those of the UAS-SfM.

The TLS has difficulty accessing the scan target and has a limited scanning angle, causing blind spots or data shadows in the acquired point clouds [24,38–40]. Therefore, the TLS shape reproducibility rate of the fill dam investigated in this study was low at 74.59%. However, when combined with the UAS-SfM point clouds, the shape reproducibility rate was 98.53%, thus enhancing the TLS data gaps.

The combination analysis was performed by combining data from two methods and reconstructing a triangular network between points. In the developed 3D point cloud, numerical values for ground settlement and heaving were improved by supplementing

information on coordinate accuracy and shape reproducibility generated by the UAS and TLS. This confirmed its applicability for maintenance based on a quantitative performance evaluation.

This study aimed to detect quantitative values for the settlement (heaving) of the fill-dam body using a 3D point cloud combining UAS images and TLS data. To minimize the impact on vegetation, which is the largest obstacle to geotechnical structures [24,52], data obtained in winter were used for the analysis. To this end, this study used UAS and TLS. However, 3D data can be collected with minimal obstacles to fill dam analysis by combining various sensors and techniques such as UAS–LiDAR, ground cameras, and LiDAR SLAM. Therefore, further research on this topic is needed.

5. Conclusions

To examine the effectiveness of 3D modeling analyses for quantitative maintenance targeting fill dams, a 3D point cloud comparing UAS photogrammetry and TLS (terrestrial LiDAR) and a 3D point cloud for combined analysis were implemented. Moreover, their accuracy and reproducibility were verified. Furthermore, the quantitative values of settlement and heaving of an existing dam body were detected and reviewed in terms of maintenance. The conclusions of this study are as follows:

1. A 3D point cloud was constructed based on image data acquired in summer and winter to review its effectiveness for the quantitative maintenance of fill dams using the UAS. The comparative analysis confirmed that data obtained in winter exhibited high efficiency.
2. In soil structures such as fill dams, the Z-coordinate error of the UAS-SfM-based 3D point cloud is larger than that of the X- and Y-coordinates. Furthermore, data gaps occurred because of obstacles such as trees. Therefore, an advanced 3D point cloud was constructed by combining it with a TLS-based 3D point cloud. In addition, the coordinate accuracies of the X-, Y-, and Z-axes were improved by combining the two datasets.
3. The TLS-based 3D point cloud exhibited a shape reproducibility of 74.59% because of occlusions such as trees and buildings, equipment access, and scanning angle. The shape reproducibility rate of the UAS-SfM-based 3D point cloud was improved to 98.53% by reconstructing it as a 3D point cloud based on the combination analysis.
4. To detect the numerical values of ground settlement and heaving, the settlement and heaving areas of a 3D point cloud based on the combination analysis were reviewed using the cross-sectional data collected from a contact survey. Consequently, ground changes in four regions of the downstream slope, seven regions of the dam crest, and four regions of the upstream slope were confirmed. Moreover, quantitative values, namely heaving and settlement volumes, were calculated.
5. This study examined the effectiveness of the UAS, TLS, and a combination analysis for 3D-model-based maintenance of fill dams. The advantages of each method were highlighted, and the effectiveness of complementing the disadvantages was verified using a data-combined 3D point cloud.

Author Contributions: J.K. (Joonoh Kang): conceptualization, methodology, software, validation, formal analysis, data curation, writing—original draft preparation, visualization; C.L.: investigation, writing—review and editing, project administration; D.K. (Daljoo Kim): funding acquisition; J.K. (Jaemo Kang): supervision; D.K. (Donggyou Kim): resources. All authors have read and agreed to the published version of the manuscript.

Data Availability Statement: The dataset used in this research is available upon a valid request to any of the authors of this research article.

References

1. Korea Authority of Land & Infrastructure Safety. *2021 Facility Statistical Yearbook*; Korea Authority of Land & Infrastructure Safety: Sejong, Republic of Korea, 2021.
2. Fathi, H.; Dai, F.; Lourakis, M. Automated as-built 3d reconstruction of civil infrastructure using computer vision: Achievements, opportunities, and challenges. *Adv. Eng. Inform.* **2015**, *29*, 149–161. [CrossRef]
3. Zhu, X.; Bao, T.; Yeoh, J.K.W.; Jia, N.; Li, H. Enhancing dam safety evaluation using dam digital twins. *Struct. Infrastruct. Eng.* **2021**, *10*, 904–920. [CrossRef]
4. El-Dim, M.N.; Pereira, P.F.; Martins, J.P.; Ramos, N.M.M. Digital Twins for Construction Assets Using BIM Standard Specifications. *Buildings* **2022**, *12*, 2155. [CrossRef]
5. Khaloo, A.; Lattanzi, D.; Jackimowicz, A.; Devaney, C. Utility UAV and 3D computer vision for visual inspection of a large gravity dam. *Front. Built Environ.* **2018**, *4*, 31. [CrossRef]
6. Zang, Y.; Yang, B.; Li, J.; Guan, H. An accurate TLS and UAV image point clouds registration method for deformation detection of chaotic hillside areas. *Remote Sens.* **2019**, *11*, 647. [CrossRef]
7. Samodra, G.; Ramadhan, M.F.; Sartohadi, J.; Setiawan, M.A.; Christanto, N.; Sukmawijaya, A. Characterization of displacement and internal structure of landslides from multitemporal UAV and ERT imaging. *Landslides* **2020**, *17*, 2455–2468. [CrossRef]
8. Yan, Y.; Ma, S.; Yin, S.; Hu, S.; Long, Y.; Xie, C.; Jiang, H. Detection and numerical simulation of potential hazard in oil pipeline areas based on UAV surveys. *Front. Earth Sci.* **2021**, *9*, 665478. [CrossRef]
9. Mancini, F.; Dubbini, M.; Gattelli, M.; Stecchi, F.; Fabbri, S.; Gabbianelli, G. Using unmanned aerial vehicles (UAV) for high-resolution reconstruction of topography: The structure from motion approach on coastal environments. *Remote Sens.* **2013**, *5*, 6880–6898. [CrossRef]
10. Liu, P.; Chen, A.Y.; Huang, Y.N.; Han, J.Y.; Lai, J.S.; Kang, S.C. A Review of rotorcraft unmanned aerial vehicle (UAV) developments and applications in civil engineering. *Smart Struct. Syst.* **2014**, *13*, 1065–1094. [CrossRef]
11. Lindner, G.; Schraml, K.; Mansberger, R.; Hübl, J. UAV monitoring and documentation of a large landslide. *Appl. Geomat.* **2015**, *8*, 1–11. [CrossRef]
12. Ma, S.; Xu, C.; Shao, X.; Zhang, P.; Liang, X.; Tian, Y. Geometric and kinematic features of a landslide in Mabian, Sichuan, China, derived from UAV photography. *Landslides* **2018**, *16*, 373–381. [CrossRef]
13. Guisado-Pintado, E.; Jackson, D.W.T.; Rogers, D. 3D mapping efficacy of a drone and terrestrial laser scanner over a temperate beach-dune zone. *Geomorphology* **2019**, *328*, 157–172. [CrossRef]
14. Lu, H.; Ma, L.; Fu, X.; Liu, C.; Wang, Z.; Tang, M.; Li, N. Landslides information extraction using object-oriented image analysis paradigm based on deep learning and transfer learning. *Remote Sens.* **2020**, *12*, 752. [CrossRef]
15. Yu, M.; Huang, Y.; Zhou, J.; Mao, L. Modeling of landslide topography based on micro-unmanned aerial vehicle photography and structure-from-motion. *Environ. Earth Sci.* **2017**, *76*, 520. [CrossRef]
16. Lee, J.; Min, S.S. Assessment of positioning accuracy of UAV photogrammetry based on RTK-GPS. *J. Korea Acad. –Ind. Coop. Soc.* **2018**, *19*, 63–68. [CrossRef]
17. Rangel, J.M.G.; Gonçalves, G.R.; Pérez, J.A. The impact of number and spatial distribution of GCPs on the positional accuracy of geospatial products derived from low-cost UASs. *Int. J. Remote Sens.* **2018**, *39*, 7154–7171. [CrossRef]
18. Jaud, M.; Bertin, S.; Beauverger, M.; Augereau, E.; Delacourt, C. RTK GNSS-assisted terrestrial SfM photogrammetry without GCP: Application to coastal morphodynamics monitoring. *Remote Sens.* **2020**, *12*, 1889. [CrossRef]
19. Mao, Z.; Hu, S.; Wang, N.; Long, Y. Precision evaluation and fusion of topographic data based on UAVs and TLS surveys of a loess landslide. *Front. Earth Sci.* **2021**, *9*, 801293. [CrossRef]
20. Yang, D.; Qiu, H.; Hu, S.; Pei, Y.; Wang, X.; Du, C.; Long, Y.; Cao, M. Influence of successive landslides on topographic changes revealed by multitemporal high-resolution UAS-based DEM. *Catena* **2021**, *202*, 105229. [CrossRef]
21. Tang, P.; Huber, D.; Akinci, B.; Lipman, R.; Lytle, A. Automatic reconstruction of as-built building information models from laser-scanned point clouds: A review of related techniques. *Autom. Constr.* **2010**, *19*, 829–843. [CrossRef]
22. Xiao, Y.; Wang, C.; Li, J.; Zhang, W.; Xi, X.; Wang, C.; Dong, P. Building segmentation and modeling from airborne LiDAR data. *Int. J. Digit. Earth* **2015**, *8*, 694–709. [CrossRef]
23. Brede, B.; Calders, K.; Lau, A.; Raumonen, P.; Bartholomeus, H.M.; Herold, M.; Kooistra, L. Non-destructive tree volume estimation through quantitative structure modelling: Comparing UAV laser scanning with terrestrial LIDAR. *Remote Sens. Environ.* **2019**, *233*, 111355. [CrossRef]
24. Šašak, J.; Gallay, M.; Kaňuk, J.; Hofierka, J.; Minár, J. Combined use of terrestrial laser scanning and UAV photogrammetry in mapping alpine terrain. *Remote Sens.* **2019**, *11*, 2154. [CrossRef]
25. Wijesingha, J.; Moeckel, T.; Hensgen, F.; Wachendorf, M. Evaluation of 3D point cloud-based models for the prediction of grassland biomass. *Int. J. Appl. Earth Obs. Geoinf.* **2019**, *78*, 352–359. [CrossRef]
26. Lee, C.-H.; Lee, J.-H.; Kim, D.-J.; Kang, J.-O.; Kwon, Y.-H. A study on damage factor analysis of slope anchor based on 3D numerical model combining UAS image and terrestrial LiDAR. *J. Korean Geotechn. Soc.* **2022**, *38*, 5–24.
27. Wefelscheid, C.; Hansch, R.; Hellwich, O. Three-dimensional building reconstruction using images obtained by unmanned aerial vehicles. *Int. Arch. Photogramm. Remote Sens. Spatial Inform. Sci.* **2011**, *XXXVIII-1*, 183–188. [CrossRef]
28. Buffi, G.; Manciola, P.; Grassi, S.; Barberini, M.; Gambi, A. Survey of the Ridracoli dam: UAV–based photogrammetry and traditional topographic techniques in the inspection of vertical structures. *Geomat. Nat. Haz. Risk* **2017**, *8*, 1562–1579. [CrossRef]

29. Korumaz, M.; Betti, M.; Conti, A.; Tucci, G.; Bartoli, G.; Bonora, V.; Güleç Korumaz, A.; Fiorini, L. An integrated terrestrial laser scanner (TLS), deviation analysis (DA) and finite element (FE) approach for health assessment of historical structures. A minaret case study. *Eng. Struct.* **2017**, *153*, 224–238. [CrossRef]

30. Martínez-Carricondo, P.; Agüera-Vega, F.; Carvajal-Ramírez, F. Use of UAV-photogrammetry for quasi-vertical wall surveying. *Remote Sens.* **2020**, *12*, 2221. [CrossRef]

31. Martínez-Carricondo, P.; Agüera-Vega, F.; Carvajal-Ramírez, F.; Mesas-Carrascosa, F.-J.; García-Ferrer, A.; Pérez-Porras, F.-J. Assessment of UAV-photogrammetric mapping accuracy based on variation of ground control points. *Int. J. Appl. Earth Obs. Geoinf.* **2018**, *72*, 1–10. [CrossRef]

32. Medjkane, M.; Maquaire, O.; Costa, S.; Roulland, T.; Letortu, P.; Fauchard, C.; Antoine, R.; Davidson, R. High-resolution monitoring of complex coastal morphology changes: Cross-efficiency of SfM and TLS-based survey (Vaches-Noires Cliffs, Normandy, France). *Landslides* **2018**, *15*, 1097–1108. [CrossRef]

33. Bakirman, T.; Bayram, B.; Akpinar, B.; Karabulut, M.F.; Bayrak, O.C.; Yigitoglu, A.; Seker, D.Z. Implementation of ultra-light UAV systems for cultural heritage documentation. *J. Cult. Herit.* **2020**, *44*, 174–184. [CrossRef]

34. Peppa, M.V.; Mills, J.P.; Moore, P.; Miller, P.E.; Chambers, J.E. Accuracy assessment of a UAV-based landslide monitoring system. *ISPRS Int. Arch. Photogramm. Remote Sens. Spat. Inf. Sci.* **2016**, *41*, 895–902. [CrossRef]

35. Lee, J.; Kang, J.; Lee, S. A study on the improvement of UAV based 3D point cloud spatial object location accuracy using road information. *Korean J. Remote Sens.* **2019**, *35*, 705–714. [CrossRef]

36. Agüera-Vega, F.; Agüera-Puntas, M.; Martínez-Carricondo, P.; Mancini, F.; Carvajal, F. Effects of point cloud density, interpolation method and grid size on derived digital terrain model accuracy at micro topography level. *Int. J. Remote Sens.* **2020**, *41*, 8281–8299. [CrossRef]

37. Moon, D.-Y. An Optimization Method to Generate 3D Earthworks World Model Using Hybrid (UAV & TLS) Point Cloud Data. Ph.D. Thesis, Sungkyunkwan University, Seoul, Republic of Korea, 2019.

38. Pellicani, R.; Argentiero, I.; Manzari, P.; Spilotro, G.; Marzo, C.; Ermini, R.; Apollonio, C. UAV and airborne LiDAR data for interpreting kinematic evolution of landslide movements: The case study of the Montescaglioso landslide (Southern Italy). *Geosciences* **2019**, *9*, 248. [CrossRef]

39. Kamnik, R.; Nekrep Perc, M.; Topolšek, D. Using the scanners and drone for comparison of point cloud accuracy at traffic accident analysis. *Accid. Anal. Prev.* **2020**, *135*, 105391. [CrossRef]

40. Tsunetaka, H.; Hotta, N.; Hayakawa, Y.S.; Imaizumi, F. Spatial accuracy assessment of unmanned aerial vehicle-based structures from motion multi-view stereo photogrammetry for geomorphic observations in initiation zones of debris flows, Ohya landslide, Japan. *Prog. Earth Planet. Sci.* **2020**, *7*, 24. [CrossRef]

41. Wang, J.; Zhang, C. Deformation monitoring of earth-rock dams based on three-dimensional laser scanning technology. *Chin. J. Geotech. Eng.* **2014**, *36*, 2345–2350. [CrossRef]

42. Hendrickx, H.; De Sloover, L.; Stal, C.; Delaloye, R.; Nyssen, J.; Frankl, A. Talus slope geomorphology investigated at multiple time scales from high-resolution topographic surveys and historical aerial photographs (Sanetsch Pass, Switzerland). *Earth Surf. Process. Landf.* **2020**, *45*, 3653–3669. [CrossRef]

43. Li, Y.; Liu, P.; Li, H.; Huang, F. A comparison method for 3D laser point clouds in displacement change detection for arch dams. *ISPRS Int. J. Geo-Inf.* **2021**, *10*, 184. [CrossRef]

44. Henriques, M.J.; Roque, D. Unmanned aerial vehicles (UAV) as a support to visual inspections of concrete dams. In Proceedings of the Second International Dam World Conference, Laboratorio Nacional De Engenharia Civil, Lisbon, Portugal, 21–24 April 2015.

45. Besl, P.J.; McKay, N.D. A method for registration of 3-D shapes. *IEEE Trans. Pattern Anal. Mach. Intell.* **1992**, *14*, 239–256. [CrossRef]

46. Balsa-Barreiro, J.; Fritsch, D. Generation of visually aesthetic and detailed 3D models of historical cities by using laser scanning and digital photogrammetry. *Digit. Appl. Archaeol. Cult. Herit.* **2018**, *8*, 57–64. [CrossRef]

47. Wu, L.; Wang, G.; Hu, Y. Iterative closest point registration for fast point feature histogram features of a volume density optimization algorithm. *Meas. Control* **2020**, *53*, 29–39. [CrossRef]

48. Mesas-Carrascosa, F.-J.; Notario García, M.D.; Meroño de Larriva, J.E.; García-Ferrer, A. An analysis of the influence of flight parameters in the generation of unmanned aerial vehicle (UAV) orthomosaicks to survey archaeological areas. *Sensors* **2016**, *16*, 1838. [CrossRef] [PubMed]

49. Lee, H.-J.; Cho, G.-S. Comparative accuracy of terrestrial LiDAR and unmanned aerial vehicles for 3D modeling of cultural properties. *J. Cadastre Land Inf.* **2017**, *47*, 1.

50. Kang, J.O.; Lee, Y.C. Construction of 3D spatial information of vertical structure by combining UAS and terrestrial LiDAR. *J. Cadastre Land Inf.* **2019**, *49*, 57–66.

51. Hayakawa, Y.C.; Obanawa, H. Volumetric change detection in bedrock coastal cliffs using terrestrial laser scanning and UAS-based SfM. *Sensors* **2020**, *20*, 3403. [CrossRef]

52. Son, S.W.; Kim, D.W.; Sung, W.G.; Yu, J.J. Integrating UAV and TLS approaches for environmental management: A case study of a waste stockpile area. *Remote Sens.* **2020**, *12*, 1615. [CrossRef]

53. Martínez-Carricondo, P.; Carvajal-Ramírez, F.; Yero-Paneque, L.; Agüera-Vega, F. Combination of HBIM and UAV photogrammetry for modelling and documentation of forgotten heritage. Case study: Isabel II dam in Níjar (Almería, Spain). *Herit. Sci.* **2021**, *9*, 95. [CrossRef]

54. Zhao, S.; Kang, F.; Li, J.; Ma, C. Structural health monitoring and inspection of dams based on UAV photogrammetry with image 3D reconstruction. *Autom. Constr.* **2021**, *130*, 103832. [CrossRef]

55. Ridolfi, E.; Buffi, G.; Venturi, S.; Manciola, P. Accuracy analysis of a dam model from drone surveys. *Sensors* **2017**, *17*, 1777. [CrossRef] [PubMed]

56. Yang, M.-D.; Huang, K.-S.; Tsai, H.-P. Monitoring and measurement of an artificial landslide dam using UAV images and image-based modeling (MCSSE). *DEStech Trans. Comput. Sci. Eng.* **2016**, 357–362. [CrossRef]

57. Ramos-Alcázar, L.; Marchamalo-Sacristán, M.; Martínez-Marín, R. Comparing dam movements obtained with terrestrial laser scanner (TLS) data against direct pendulums records. *Rev. Fac. Ing. Univ. Antioq.* **2015**, *76*, 99–106. [CrossRef]

58. Ramos-Alcázar, L.; Marchamalo-Sacristán, M.; Martínez-Marín, R. Estimating and plotting TLS midrange precisions in field conditions: Application to dam monitoring. *Int. J. Civ. Eng.* **2017**, *15*, 299–307. [CrossRef]

59. Scaioni, M.; Marsella, M.; Crosetto, M.; Tornatore, V.; Wang, J. Geodetic and remote-sensing sensors for dam deformation monitoring. *Sensors* **2018**, *18*, 3682. [CrossRef]

60. Zhang, J.; Lin, X. Advances in fusion of optical imagery and LiDAR point cloud applied to photogrammetry and remote sensing. *Int. J. Image Data Fus.* **2017**, *8*, 1–31. [CrossRef]

61. Ministry of Land, Infrastructure and Transport. *Special Act on the Safety Control and Maintenance of Establishments*; KIRL: Sejong, Republic of Korea, 2021.

62. Ji, H.; Luo, X. 3D scene reconstruction of landslide topography based on data fusion between laser point cloud and UAV image. *Environ. Earth Sci.* **2019**, *78*, 534. [CrossRef]

63. Agüera-Vega, F.; Carvajal-Ramírez, F.; Martínez-Carricondo, P. Accuracy of digital surface models and orthophotos derived from unmanned aerial vehicle photogrammetry. *J. Surv. Eng.* **2016**, *143*, 4016025. [CrossRef]

64. Pepe, M.; Fregonese, L.; Scaioni, M. Planning airborne photogrammetry and remote-sensing missions with modern platforms and sensors. *Eur. J. Remote Sens.* **2018**, *51*, 412–436. [CrossRef]

65. Mikhail, E.; Bethel, J.; McGlone, J. *Introduction to Modern Photogrammetry*; John Wiley & Sons: New York, NY, USA, 2001; p. 496.

66. Fraser, C.S. *Network Design. Close Range Photogrammetry and Machine Vision*; Atkinson, K.B., Ed.; Whittles Publishing: Caithness, Fingland, 1996; pp. 256–281.

67. Aber, J.; Marzolff, I.; Ries, J.B. *Small Format Aerial Photography: Principles, Techniques and Geoscience Applications*; Elsevier: Amsterdam, The Netherlands, 2016; p. 394.

68. Sanz-Ablanedo, E.; Chandler, J.H.; Rodríguez-Pérez, J.R.; Ordóñez, C. Accuracy of unmanned aerial vehicle (UAV) and SfM photogrammetry survey as a function of the number and location of ground control points used. *Remote Sens.* **2018**, *10*, 1606. [CrossRef]

69. Neugirg, F.; Stark, M.; Kaiser, A.; Vlacilova, M.; Della Seta, M.; Vergari, F.; Schmidt, J.; Becht, M.; Haas, F. Erosion processes in Calanchi in the Upper Orcia Valley, Southern Tuscany, Italy based on multitemporal high-resolution terrestrial LiDAR and UAV surveys. *Geomorphology* **2016**, *269*, 8–22. [CrossRef]

70. Coveney, S.; Roberts, K. Lightweight UAV digital elevation models and orthoimagery for environmental applications: Data accuracy evaluation and potential for river flood risk modelling. *Int. J. Remote Sens.* **2017**, *38*, 3159–3180. [CrossRef]